Improved work hardening capability and ductility of an additively manufactured and deformed Al-Mn-Mg-Sc-Zr alloy

Daniel Schliephake[a], Christophe Lopes[a,b], Yolita M. Eggeler[b], Hans Chen[c,1], Jens Freudenberger[d,e], Dina Bayoumy[f], Aijun J. Huang[f], Alexander Kauffmann[a,*]

[a] Institute for Applied Materials (IAM-WK), Karlsruhe Institute of Technology (KIT), Engelbert-Arnold-Str. 4, D-76131 Karlsruhe, Germany

[b] Microscopy of Nanoscale Strcutures & Mechanisms (MNM), Laboratory for Electron Microscopy (LEM), Karlsruhe Institute of Technology (KIT), Engesserstr. 7, D-76131 Karlsruhe, Germany

[c] Institute for Technical Physics (ITEP), Karlsruhe Institute of Technology (KIT), Hermann-von-Helmholtz-Platz 1, D-76344, Eggenstein-Leopoldshafen, Germany

[d] Leibniz Institute for Solid State and Materials Research Dresden (IFW Dresden), Helmholtzstr. 20, D-01069, Dresden, Germany

[e] Institute of Materials Science, Technische Universität Bergakademie Freiberg, Gustav-Zeuner-Str. 5, D-09599 Freiberg, Germany

[f] Monash Centre for Additive Manufacturing (MCAM), Monash University, 15-17 Normanby Rd, Notting Hill, VIC 3168, Australia

*corresponding author: alexander.kauffmann@kit.edu

Keywords high-strength Al alloy, laser powder bed fusion, cold working, mechanical properties, precipitation strengthening

Abstract

An Al-Mn-Mg-Sc-Zr alloy was additively manufactured and deformed by rotary swaging to investigate the effect of high defect densities on the precipitation behavior, work hardening capability and ductility. For this, the LPBF-fabricated alloy was deformed by rotary swaging up to a true strain of 2.5 subsequent to a laser powder bed fusion (LPBF) process. Compared to the LPBF condition, swaging results in a refinement of the microstructure by one order of magnitude and an increased hardness and ultimate tensile strength (UTS) which is mainly attributed to the finer microstructure of the swaged alloy. By annealing, a higher peak-aging hardness of (209 ± 2) HV0.1 and UTS of (717 ± 2) MPa of the swaged alloy at a lower peak-aging temperature of 300 °C (1 h) was obtained. Significant improvement of uniform elongation by enhanced work hardening capability of the swaged and annealed alloy is obtained for annealing temperatures above 300 °C while strength is only moderately affected. The significant improvement of aging kinetics is discussed alongside a profound microstructural characterization of the heterogeneous grain structure and precipitate distribution.

[1] now with: Vacuumschmelze GmbH & Co. KG, Grüner Weg 37, 63450 Hanau, Germany

1. Introduction

In recent years, the increased use of additive manufacturing (AM) in general, and laser powder bed fusion (LPBF) in particular, has led to the development of several new age-hardening, high-strength aluminum alloys that can only be processed by utilizing this technology. Scalmalloy® probably is the most prominent alloy, which is based on the Mg-containing 5*xxx* series and is modified by Sc and Zr additions [1-3]. The 0.2% offset yield strength for Al-5Mg increases from 115 MPa to 266 MPa by minor additions of Sc and Zr of 0.2 and 0.1 wt.%, respectively [4]. The increase in strength is mainly associated with precipitate strengthening by $L1_2$-ordered $Al_3(Sc,Zr)$ particles and grain boundary strengthening as a result of the fine microstructure due to the primary solidification of the $Al_3(Sc,Zr)$ particles that further act as heterogeneous nucleation [5,6]. It is worth noticing, that grain refinement in binary Al-Sc alloys is usually observed at higher Sc contents beyond 0.5 wt.%, but Zr noticeably reduces the necessary amount of Sc for grain refinement [4,7]. Zr is known to substitute Sc atoms in the Al_3Sc phase [8,9]; for simplicity we, therefore, refer to Al_3Sc in this manuscript. The maximum amount of Sc, which can be effectively used for age-hardening in casted Al-Sc alloys is limited by its maximum solubility of 0.3 wt.% [10]. However, due to the high cooling rates of up to 10^6 K/s associated with LPBF [11,12], the solubility of Sc in the super-saturated solid solution increases to 0.7 wt.% [1,13]. The higher cooling rates compared to conventional casting processes and the higher Sc content further refine the microstructure and increases the strength of the alloys manufactured by LPBF [2,3]. The yield strength of Scalmalloy® with a nominal composition of Al-4.6Mg-0.66Sc-0.42Zr-0.49Mn (all compositions are given in wt.%, unless specified otherwise) manufactured by LPBF is 288 MPa in the as-LPBF condition and increases to 450 MPa after applying a direct aging heat treatment at 325 °C for 4 h [2]. Total elongation in the as-LPBF condition and after direct aging have been determined to be 16 % and 9 %, respectively [14]. Jia et al. [15] have modified the Mn-containing 3*xxx* series with Sc and Zr additions, to further increase solid solution strengthening. The yield strength was determined to be 438 MPa and 556 MPa in the as-LPBF and age-hardened condition, respectively [14]. Besides the increase in strength, alloying with Sc and Zr also improves the resistance against recrystallization [7,16]. Due to the thermal stability of the precipitates and microstructure, Al-Mn-Mg-Sc-Zr alloys exhibit exceptional high creep resistance at 250 °C in comparison to other precipitate-strengthened Al alloys [17].

The LPBF process usually leads to the formation of a heterogeneous microstructure as a result of the thermal gradient in the melt pool and its surroundings [18]. The microstructure consists of fine equiaxed grains at the bottom of the melt pool and columnar grains oriented in solidification direction on top of them [18]. Recently, Jia et al. [15] investigated the precipitation kinetics of an LPBF processed Al-Mn-Mg-Sc-Zr alloy and found that the heterogeneous microstructure remains stable even after annealing at 450 °C for 24 h due to the thermal stability and grain growth inhibition capability of Al_3Sc and Al_6Mn particles. Furthermore, the respective activation energies determined for the formation of Al_3Sc and Al_6Mn were found to be considerably lower than for long-range volume diffusion of Sc and Mn in Al, which is attributed to the high dislocation density within the fine-grained microstructure. However, heterogeneous microstructures can lead to limited uniform strain by localized deformation in the early stages of deformation, which can be seen in the ultimate tensile strength (UTS) occurring early at 1 to 2 % plastic strain (uniform elongation) followed by a significantly lower flow stress of Al-Mn-Sc alloys manufactured by LPBF [14,15,19,20].

To obtain a more homogenous microstructure for suppression of localized deformation and improvement of uniform strain, a cold working process with subsequent annealing to recover/recrystallize the alloy is applied in the present study. Furthermore, the LPBF process was utilized to increase the amount of precipitates by the increased supersaturation in Mn and Sc. The influence of heat treatment conditions on superimposed precipitation, recovery and recrystallization is studied with respect to microstructure and mechanical properties. The following questions were

addressed: (i) How do deformation induced defects alter the precipitation kinetics and (ii) how does the microstructure evolves after heat treatment and influence the mechanical behavior?

2. Experimental

Al-4.58Mn-1.24Mg-0.91Sc-0.42Zr powder was used to manufacture 200 mm long bars of hexagonal cross section and 10 mm in width. The composition of the powder was determined by inductively coupled plasma optical spectroscopy (ICP-OES) previously in Ref. [19]. The bars were built horizontally on the build plate by LPBF using an EOS M 290 machine. The particle size of the powder is ranging from 20 to 70 µm with an average particle size of around 35 µm. To ensure a relative density above 99.8 %, laser power, scanning speed, hatch distance and layer thickness were set to 350 W, 1600 mm/s, 0.1 mm and 0.03 mm, respectively. The scan strategy included a snake-like pattern with scan track rotation of 67° alternating between consecutive layers. LPBF was performed under Ar atmosphere. Further details on the manufacturing process and parameter optimization can be found elsewhere [19]. Subsequently, the LPBF-fabricated bars were deformed down to 3 mm in diameter via rotary swaging, applying an areal reduction of approximately 20 % per step. The totally applied true strain is 2.5. In the following, the different manufacturing conditions of the alloy are referred to as LPBF and swaged.

Microstructural characterization was carried out on samples prepared by water-cooled grinding with SiC paper as fine as grit P4000. Samples were polished using 3 and 1 µm diamond suspension before final polishing with a colloidal silica solution. Scanning electron microscopy (SEM) with backscattered electron contrast (BSE) was conducted using a JEOL 7001 FEG and FEI Apero S at 10 kV acceleration voltage. Electron backscatter diffraction (EBSD) was performed on a Zeiss Auriga 60 SEM equipped with an EDAX DigiView EBSD system. The samples for transmission electron microscopy (TEM) were prepared perpendicular to the wire axis and the slices were ground and polished to a thickness of approximately 100 µm. Subsequently, double jet electrochemical thinning was performed at temperatures of -10 °C using a mixture of electrolyte A1 and A2 (Struers). TEM micrographs were taken using an FEI Titan^3 80-300and a Philips CM 200 FEG at an acceleration voltage of 300 kV and 200 kV, respectively. Elemental mapping was performed at the FEI Osiris ChemiStem equipped with a SuperX detector using scanning transmission electron microscopy (STEM) and energy-dispersive x-ray spectroscopy (EDXS) operated at an acceleration voltage of 200kV and quantified with the Esprit software by Bruker. All microstructural characterization of the swaged alloy was done on the normal surface to the cross section with the wire direction (WD) out of projection plane. Grain size distribution of the alloy and volume fraction of additional phases were determined by image analysis. While the interception method was used to estimate the grain size distribution in the different region of the swaged alloy using TEM images, the areal fraction of the phases was determined in the software ImageJ based on SEM micrographs. The equivalence of areal fraction and volume fraction was considered assuming isometry and isotropy of the investigated microstructural features.

Annealing experiments of the LPBF and swaged condition were performed using a box furnace by Nabertherm. Specimens of each condition were (i) annealed at 300°C for various times ranging from 15 min to 360 min and (ii) annealed for one hour at various temperatures ranging from 250°C to 550°C. Subsequent to the aging treatment, all specimens were water-quenched. Hardness of the alloy after various aging treatments was measured using a Qness Q10+ microhardness tester at HV0.1. A 100 kN Instron 5982 machine was utilized for tensile tests on the LPBF alloy and tensile samples were machined from hexagonal rods with a cross-section of 10 mm manufactured horizontal to the build plate. The gauge length of the specimens was 24 mm with a diameter of 6 mm. Tensile tests on the swaged alloy were performed using a ZwickRoell universal testing machine equipped with an optical extensometer system VideoXtens by ZwickRoell. Tensile samples were directly cut from the swaged material with a total length of 175 mm and a gauge length of 50 mm observed by the VideoXtens

system and were subject to a heat treatment at 300, 375 and 550 °C and subsequently water quenched, except for the tensile samples that remained in the as-swaged condition. The initial strain rate for the displacement controlled tensile testing of both conditions, LPBF and swaged, was $4.8 \cdot 10^{-4}$ s^{-1}. At least three samples were tested on each manufacturing and annealing condition.

X-ray diffraction (XRD) was performed on longitudinal sections of the swaged and annealed wires using a D2 Phaser by Bruker equipped with a LynxEye line detector. The scanning was carried out in Bragg-Brentano geometry on polished surfaces in 0.01° steps with a Cu X-ray tube operating at 30 kV and 10 mA. The according radiation was filtered by means of Ni foil. Lattice parameters were determined by extrapolating the peak positions using a Nelson-Riley approach [21]. In order to estimate the contribution by internal lattice strain, peak width $\Delta 2\Theta$ in the diffraction patterns as a function of peak position 2Θ were used and expressed in terms of the scattering vector $\Delta s = \frac{\Delta 2\Theta \cos\Theta}{\lambda}$ and $s = \frac{2\sin\Theta}{\lambda}$, respectively. λ was 1.5406 Å. Instrumental broadening (analysis of an LaB_6 reference powder) was subtracted in order to obtain Δs. Due to low elastic anisotropy, linear trends are observed for Δs vs. s (Williamson-Hall plot) for all processing conditions in this study (see Supplementary Material S2). The slope m of the linear relationship is considered dominated by dislocation density ρ subsequent to rotary swaging due to low density of other defects contributing to internal lattice strain in the present materials conditions (for example stacking fault due to high stacking fault energy of Al based alloys). As a rough estimate, dislocation density ρ scales with $m \propto \sqrt{\rho}$ [22].

3. Results

3.1 Initial microstructure

The initial microstructures of the LPBF and swaged condition have been investigated by means of SEM and TEM. Fig. 1a displays the bimodal initial microstructure of the LPBF alloy along the solidification direction. It consists of a fine-grained (FG) region with equiaxed grains at the bottom of the melt-pool with grain sizes of (0.49 ± 0.05) µm and coarse elongated grains (CG) in the center and top region of the melt-pool. The elongated grains with up to 50 µm are arranged in a fan-shape morphology along the solidification direction with an aspect ratio of approx. ten. Higher magnification SEM micrographs of FG and CG show additional phases at the grain boundaries and within the grains in Fig. 1b in the upper right and lower left corner, respectively. These phases have previously been identified as $L1_2$ Al_3Sc and quasicrystalline Al_6Mn [19]. The total volume fraction of both phases is (6.9 ± 0.6) vol.% in FG, while it is (2.2 ± 0.3) vol.% in CG. No attempt was undertaken in this work to distinguish between the two phases due to similar atomic Z contrast. After swaging, the microstructure remains bimodal as can be seen in Figs. 1c and d. Comparison of Fig. 1a and 1c illustrates that the size of the fan-shaped regions, tagged by the dashed line, is smaller after swaging. Furthermore, the grain size of the equiaxed grains in FG after swaging is (0.10 ± 0.05) µm. For CG, the length of the elongated grains is (2.8 ± 1.3) µm, while the aspect ratio remains similar to the LPBF condition at approx. ten with a mean grain width of (0.26 ± 0.12) µm. The determined volume fraction of the additional phases Al_3Sc and Al_6Mn after swaging compared to the as-LPBF condition is (2.3 ± 0.5) vol.% and (5.8 ± 1.1) vol.% for CG and FG, respectively. Therefore, no significant change was observed in the SEM and TEM investigations subsequent to swaging. The varying contrast within single grains in high angle annular dark-field (HAADF) STEM images in Fig. 1d displays the two additional phases (marked by arrows) and the high dislocation density after swaging. The secondary phases have been again identified as Al_3Sc of $L1_2$ crystal structure and Al_6Mn of a ten-fold quasicrystalline structure (see Supplemental Material Fig. S1a-d), which were also found in the LPBF condition. Even though severe deformation can lead to dissolution of precipitates [23], no change in volume fraction of the additional phases was detected after cold working within the resolution of the applied microscopy techniques and for the comparably lower true strains ((5.8 ± 1.1) vol.% for FG and (2.3 ± 0.5) vol.% for CG).

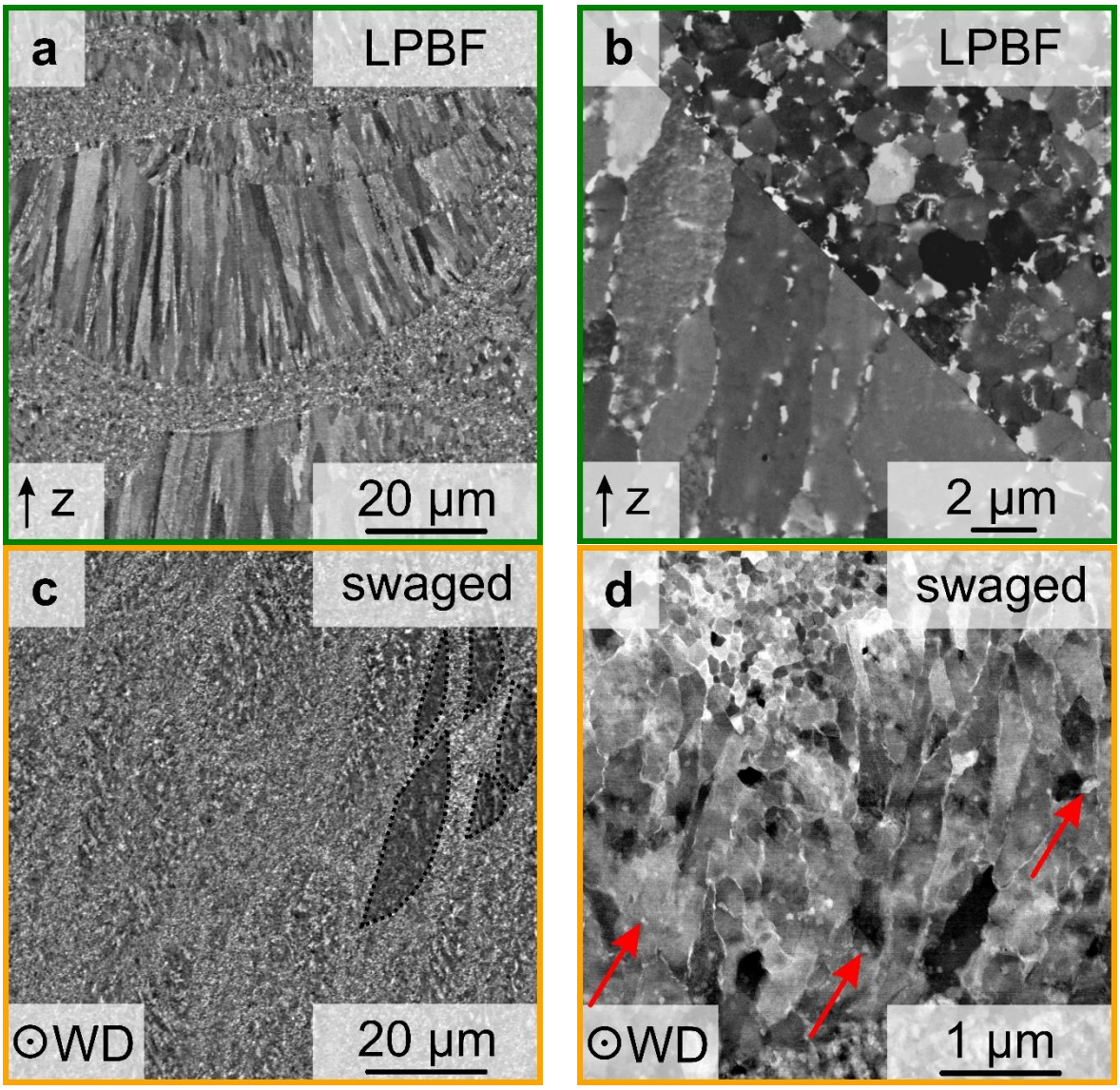

Figure 1: Microstructure of Al-4.58Mn-1.24Mg-0.91Sc-0.42Zr: (a) BSE micrograph of the LPBF condition with z denoting the build direction, (b) detailed BSE micrographs of FG (upper right corner) and CG (lower left corner) of the LPBF condition, (c) BSE micrograph after swaging with WD out of plane of projection and (d) STEM-HAADF micrograph after swaging. In (a) and (b) the z is vertical in the image and WD in (c) and (d) points out of projection plane.

3.2 Age-hardening response and mechanical properties

The aging behavior of the alloy in both fabricated conditions was investigated in terms of hardness (i) as a function of time at 300 °C and (ii) as a function of temperature for 1 h. The first case is displayed in Fig. 2a. The hardness in the as-fabricated condition after swaging is increased compared to the LPBF condition. Furthermore, the maximum hardness after annealing is determined after shorter annealing times compared to the LPBF alloy (1 h vs. 6 h). Moreover, the maximum hardness of the swaged alloy is significantly higher than for the LPBF condition with (209 ± 2) HV0.1 vs. (192 ± 3) HV0.1. Fig. 2b shows the hardness as a function of temperature at a constant annealing time of 1 h. For the swaged condition, the maximum hardness is obtained at 300 °C, while for the LPBF alloy the peak is found at 325 °C, corresponding to hardness values of (209 ± 2) HV0.1 vs. (194 ± 3) HV0.1, respectively. In case of the swaged alloy, the hardness drop is larger compared to the LPBF alloy when annealed at the same temperature beyond the peak temperature.

Tensile test specimens in the peak-aged condition at 300 °C of the LPBF and swaged alloy as well as over-aged specimens at 375 and 550°C of the swaged alloy were prepared for further mechanical testing. In addition, we tested the LPBF alloy in the peak-aged condition at 350 and 400 °C for 4 and

3 h, respectively, according to the age-hardening results reported elsewhere [15]. Fig. 2c displays the stress-strain curves of selected heat treatment conditions of the swaged and LPBF alloy. For clarity, only one test per condition is shown even though at least three samples were tested for each condition. The offset yield strength $\sigma_{0.2}$, ultimate tensile strength σ_{UTS}, uniform elongation ε_{u} and plastic strain to failure ε_{p} are summarized in Tab. 1. While the strength of the alloy increases significantly by swaging, its plastic strain drops to almost zero. The strength increases for both conditions after their respective peak age heat treatment (at 300 °C for 1 h or 6 h, see Fig. 2a), while the strength slightly decreases for the peak-aged conditions at 350 and 400 °C of the LPBF material. All conditions obtained directly from LPBF without cold working showed their maximum strength after very small plastic deformation followed by an extended plastic strain at a lower flow stress indicative of localized deformation, e.g. band formation and propagation. Furthermore, the LPBF alloy exhibits less plastic strain by increasing the annealing temperature, while for the swaged condition the plastic strain to failure improves but remains smaller compared to the LPBF condition except for the swaged 550 °C alloy. Increasing the annealing temperature for the swaged alloy further increases plastic strain, while decreasing the strength of the alloy. Besides increase in plastic strain to failure, the uniform elongation substantially increases with increasing annealing temperature in the swaged alloy. Note, ε_{u} cannot be accurately determined for the as-fabricated swaged alloy, because all samples failed in the grip section of the samples before necking occurred. In contrast to the swaged alloy, ε_{u} does not depend on the annealing treatment in the LPBF alloy except for annealing at 400 °C, where it decreased significantly. Both, hardness and σ_{UTS} follow the same trend upon annealing, as shown in Fig. 2d. From the hardness and ultimate tensile strength at various annealing temperatures a linear correlation of the two properties was obtained, following:

$$\sigma_{\mathrm{UTS}} = 4.1\ \mathrm{MPa} \cdot HV0.1 - 93\ \mathrm{MPa} \tag{1}$$

with an adjusted $R^2_{\mathrm{adj}} = 0.99$, where $HV0.1$ is the corresponding hardness value (no unit). Eq. (1) is strictly only valid for the observed hardness range of 100 to 220 HV0.1.

Table 1: Summary of offset yield strengths $\sigma_{0.2}$, UTS σ_{UTS}, strains to failure ε_p and uniform elongation ε_{u} for all tested specimen conditions incl. standard deviations obtained from sets of individual tests.

Specimen condition		$\sigma_{0.2}$ in MPa	σ_{UTS} in MPa	ε_{u} in %	ε_{p} in %
LPBF	as-LPBF	438 ± 4.1	450 ± 2	0.34 ± 0.05	19.4 ± 1
	300 °C/6 h	619 ± 1	629 ± 1	0.36 ± 0.01	11 ± 0.2
	350 °C/4 h	597 ± 1	601 ± 1	0.34 ± 0.04	9.7 ± 0.5
	400 °C/3 h	547 ± 5	549 ± 4	0.27 ± 0.02	6.5 ± 0.2
swaged	as-swaged	700 ± 3	705 ± 6	n/a	< 0.3
	300 °C/1 h	709 ± 2	717 ± 2	0.46 ± 0.05	1.1 ± 0.2
	375 °C/1 h	587 ± 10	612 ± 9	1.4 ± 0.2	2 ± 0.3
	550 °C/1 h	248 ± 7	354 ± 1	9.6 ± 0.7	10 ± 0.2

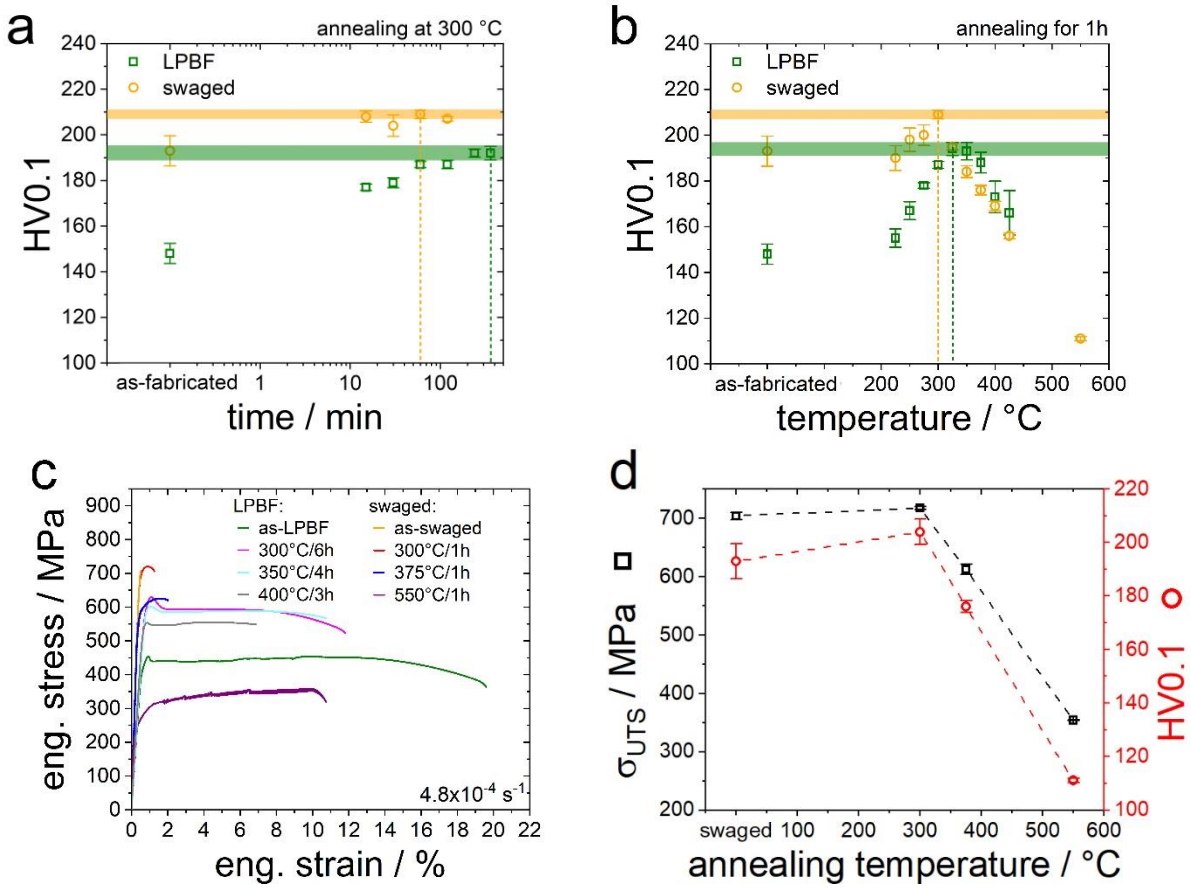

Figure 2: Summarizing the mechanical properties in terms of (a) HV0.1 after annealing for different durations at 300 °C, (b) HV0.1 after annealing at different temperatures for 1 h, (c) engineering stress-strain-curves for selected processing and annealing conditions and (d) the UTS and HV0.1 at different annealing conditions of the swaged alloy. Dashed lines and shaded regions correspond to peak-age conditions.

3.3 Characterization of swaged and annealed microstructure

In Fig. 3, EBSD maps color-coded according to the inverse pole figure (IPF) of the WD are plotted with WD out of the projection plane for the swaged condition in the different annealing conditions. The IPF map of as-swaged condition is presented in Fig. 3a, while Fig. 3b through 3c displays the alloy annealed for 1 h at 300, 375 and 550 °C, respectively. All conditions exhibit strong ⟨111⟩ and ⟨100⟩ fiber texture components being typical of wire deformation by drawing or rotary swaging of face centered cubic metals and alloys [24,25]. The heterogeneous microstructures endure for annealing up to 375 °C and becomes fully equiaxed after annealing at 550 °C. However, the microstructure remains fine-scaled and only slightly coarsens.

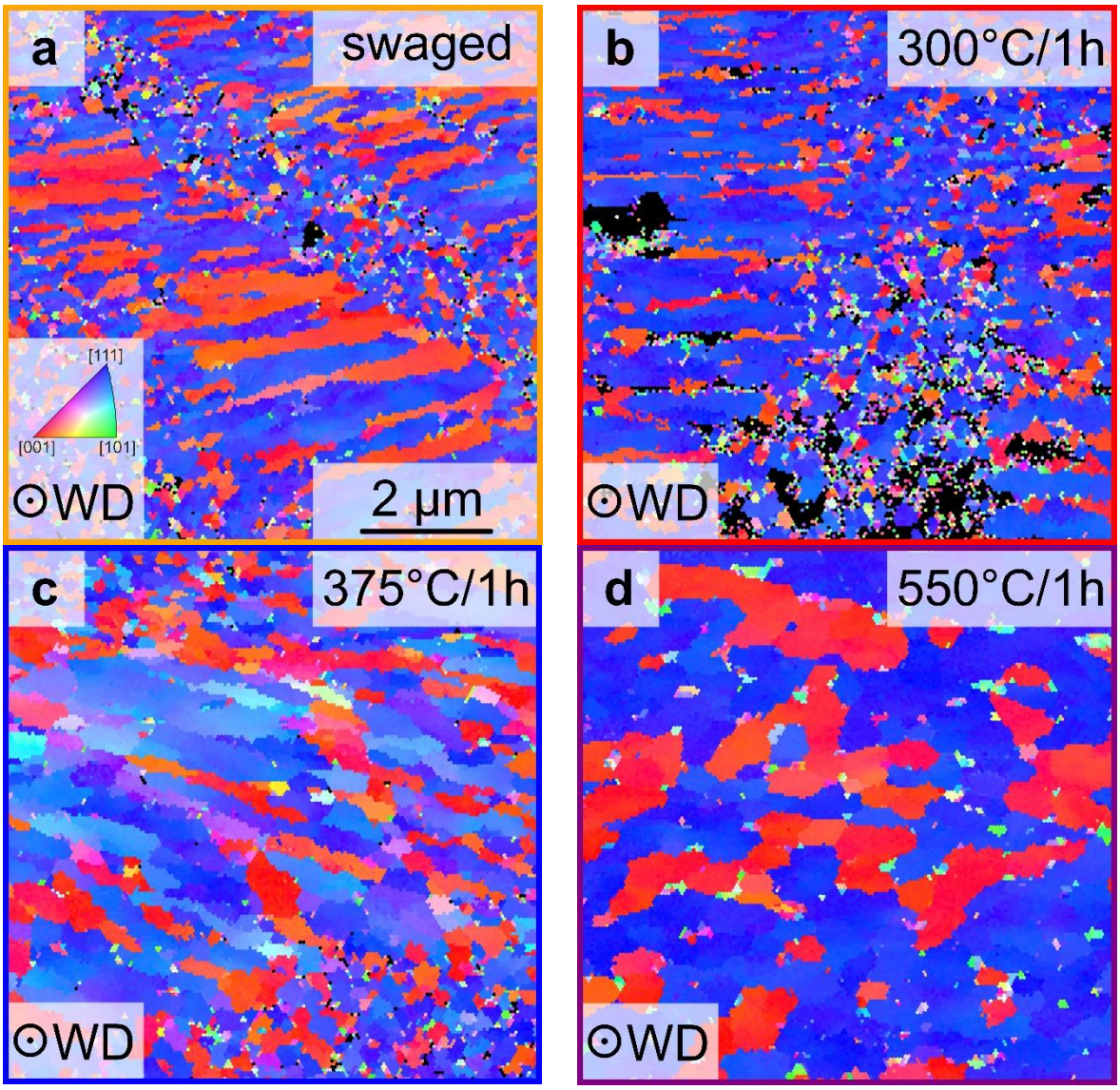

Figure 3: Orientation mapping by EBSD according to the IPF of the WD projection out of plane of (a) the as-swaged condition and following annealing for 1 h at: (b) 300 °C, (c) 375 °C and (d) 550 °C. Scale bar and color code IPF in (a) are representative for all images.

The microstructure after annealing at 300 and 375 °C has been further investigated by means of TEM in bright field (BF) mode and is shown in Figs. 4a and c, while the 550 °C condition was examined by SEM in Fig. 4e (Fig. S2 in the Supplemental Material illustrates the comparison with the swaged condition). In contrast to the 300 °C condition, grains without dislocation networks were found in the 375 °C alloy (see Fig. 4c marked by blue arrows). The corresponding EDS maps for Sc and Mn are shown in Figs. 4b and d. The microstructure in all annealed conditions remains bimodal, except for the 550 °C condition, as can be seen in Fig. 3. Fig. 5 displays the grain size distribution for the swaged alloy and after annealing at 300 and 375 °C. All changes in grain size after annealing at 300 and 375 °C are within the standard deviation and therefore not significant. The grain size after annealing in the equiaxed grain regions is (0.1 ± 0.05) and (0.16 ± 0.08) µm for 300 and 375 °C, respectively. Columnar grains exhibit widths of (0.38 ±0.15) and (0.33 ± 0.11) µm and lengths of (3.86 ± 1.56) and (2.94 ± 1.04) µm for annealing at 300 and 375 °C, respectively. The only significant change in grain size was observed after annealing at 550 °C for 1 h with an equiaxed grain size of (0.88 ± 0.11) µm. The volume fraction of Al_3Sc and Al_6Mn in the swaged alloy increases by annealing at 300 °C for 1 h from (2.3 ± 0.5) vol.% and (5.8 ± 1.1) vol.% to (9.5 ± 1) vol.% and (15.1 ± 1.3) vol.% for FG and CG, respectively. Annealing at 375 °C further increases the volume fraction of additional phases to (16.1 ± 2.8) vol.% and (19.6 ± 2.6) vol.% in FG and CG, respectively. In the alloy annealed at 375 °C, the formation of needle

shaped Al_6Mn was observed (see Fig. 4c, marked by black arrow). However, no further increase was observed after annealing at 550 °C for 1 h in the fully recrystallized microstructure with a combined volume fraction of Al_3Sc and Al_6Mn of (18.1 ± 3.5) vol.%. The bright particles in Fig. 4e are both Al_3Sc and Al_6Mn.

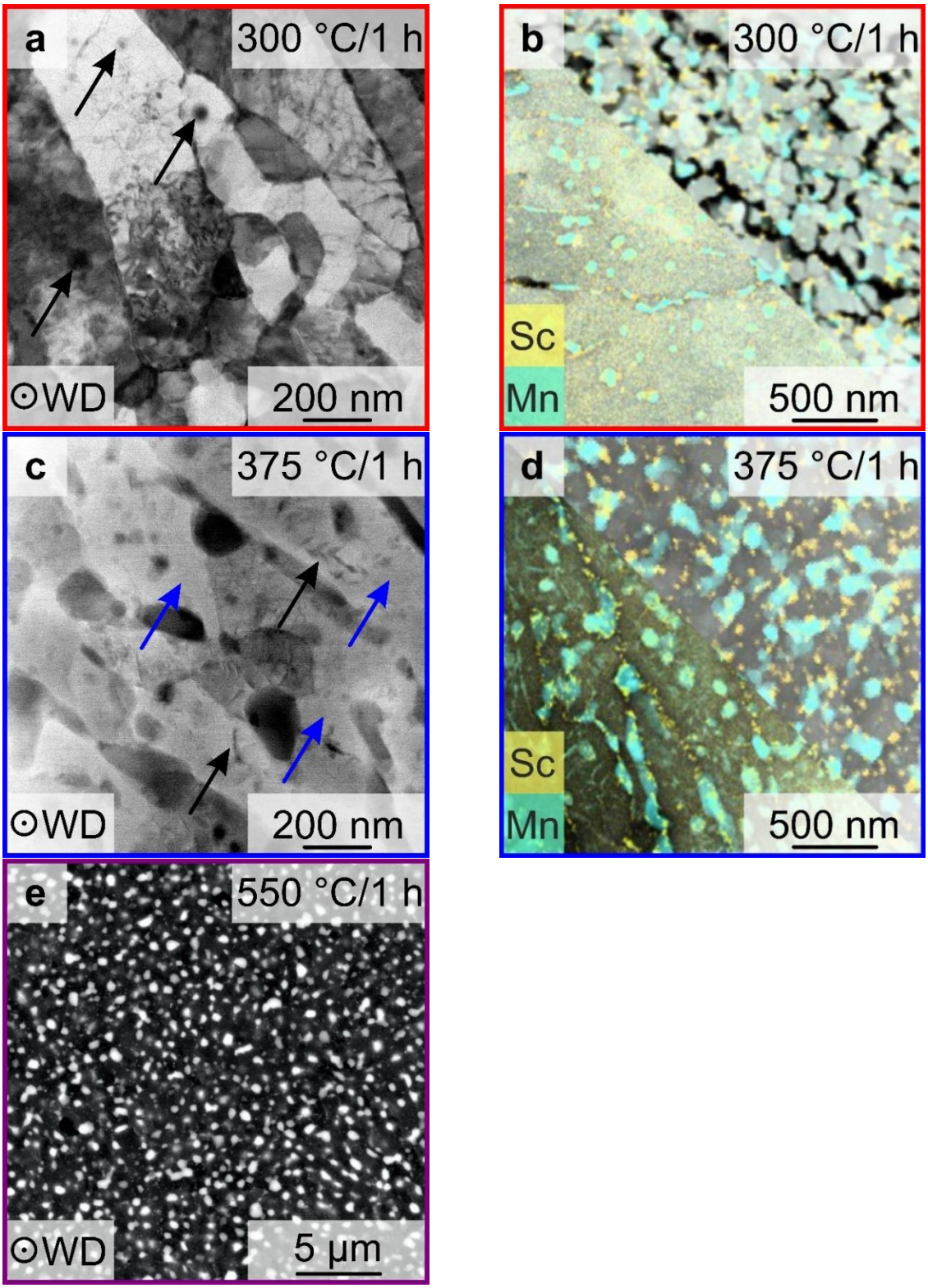

Figure 4: Microstructure of the annealed condition after swaging: (a) TEM-BF 300 °C/1 h (black arrows indicating Al_6Mn), (b) superposition of TEM-BF and EDS map 300 °C/1 h (equiaxed grain region in the upper right corner and elongated grain region in the lower left corner), (c) TEM-BF 375 °C/1 h (black arrows indicating needle-shaped Al_6Mn, blue arrows indicating recovered grains), (d) EDS map 375 °C/1 h (equiaxed grain region in the upper right corner and elongated grain region in the lower left corner), (e) BSE 550 °C/1h with WD out of projection plane.

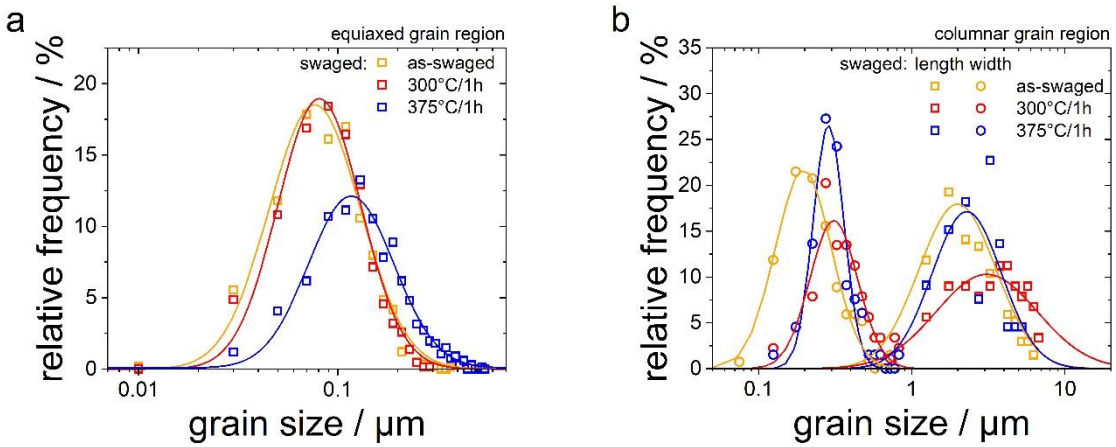

Figure 5: Summary of grain size distributions in (a) the equiaxed and (b) columnar grain regions of the swaged and annealed conditions. Continuous lines correspond to log-bimodal fits to the data.

The lattice parameter of the Al-rich solid solution calculated via the Nelson-Riley approach and the slope m determined from Williamson-Hall plots (see Supplemental Material Fig. S3) for the LPBF, swaged and heat-treated conditions are plotted in Fig. 6. Aging at 375 °C leads to a significant increase of the lattice parameter, while it remained similarly low during other processing conditions, namely LPBF, swaged and the heat treatment at 300 °C. Annealing at higher temperatures does not affect the lattice parameter any further. The internal lattice strain represented by the slope m increases by swaging and remains constant within the estimate ranges by annealing at 300 °C. Annealing at higher temperatures results in a significant decrease of m even though no significant difference between the microstructure of the samples annealed at 375 and 550 °C has been observed.

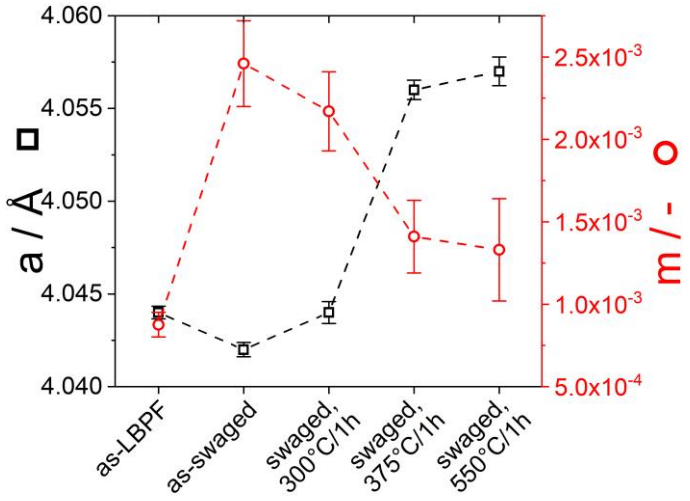

Figure 6: Dependence of lattice parameter and internal lattice strains represented by m for the various processing conditions.

4. Discussion

4.1 Microstructural evolution during swaging and annealing

The fine microstructure and the mechanical properties of the swaged alloy are a result of (i) the applied straining to the microstructure, effectively reducing the cross section of grains, (ii) recovery of the microstructure [26-29] and possibly (ii) dynamic recrystallization [27]. The geometrical grain size reduction by a true strain of 2.5 during cold work results in an average grain size of 0.15 µm for the FG region and 15 and 1.5 µm for length and width of the grains in the CG region, respectively. This is considerable larger than the observed grain sizes, see Fig. 5. Therefore, some microstructural refinement will be a result of dynamic recovery and recrystallization. In case of Al alloys, recovery might

be the dominant mechanism due to the high stacking fault energy, which promotes cross slip and subsequent annihilation of dislocations. For this reason, complete dynamic recrystallization by cold deformation is limited to high purity Al [30], which is not the case here considering the amount of alloying elements. Interestingly, the grain refinement in FG and CG is in the same order of magnitude suggesting that the different volume fractions of Al_6Mn and Al_3Sc in both regions do not affect the recovery behavior in this alloy. One reason could be, that the formation of nano-sized precipitates embedded in the matrix with similar scattering potential during deformation in both regions was not observed with the microscopy techniques used in this work. Furthermore, the dissolved amount of alloying elements is similar in FG and CG of the LPBF alloy, as recently reported in Ref. [20] for the same alloy as in the present study. At the same time, a preferred grain orientation occurs which is typical of fcc metals and alloys deformed by wire drawing or rotary swaging [24,25], while for the LPBF alloy no significant preferred grain orientation has been reported in literature so far [14,19]. However, the microstructure remains heterogeneous, which can be associated to (i) high number of particles (Al_3Sc and Al_6Mn), (ii) an uneven distribution of particles in the equiaxed and columnar regions, (iii) stable precipitates due to limited temperature increase during swaging and (iv) high dislocation density in the as-LPBF and swaged alloy. Even though the estimated internal lattice strain (which might be considered dominated by dislocation density in the present case) in the LPBF is lower compared to the swaged alloy (see Fig. 6), dislocation density in LPBF alloys is higher than in alloys obtained by conventional cast metallurgy due to the cyclic thermal processing during the layer-by-layer production of the alloys [15,31].

The fine microstructure is stable up to 375 °C, which agrees with the observations on a similar alloy of composition of Al-4.52Mn-1.32Mg-0.79Sc-0.74Zr-0.05Si-0.07Fe manufactured by LPBF by Jia et al. [15]. The heterogeneous microstructure in this LPBF alloy remained unaffected even after annealing at 450 °C and the grain size in the FG region did not change. However, a significant change of electrical conductivity was observed after annealing at 350 °C and above. This was linked to the formation of quasi-crystalline and needle-shaped Al_6Mn particles identified by TEM investigations [15]. In this work, the formation of needle-shaped Al_6Mn was not observed at 300 °C, indicating that the higher defect density in the swaged alloy prevents the nucleation of Al_6Mn precipitates at lower temperatures. The volume fraction of Al_3Sc and Al_6Mn after annealing at 300 °C has significantly increased compared to the as-fabricated swaged alloy, while in the LPBF alloy the change in volume fraction is negligible at 300 °C [17]. Therefore, the higher defect density in the swaged condition facilitates the formation of Al_3Sc and the growth of Al_6Mn. In the swaged alloy annealed at 375 °C, needle-shaped Al_6Mn precipitates were found, but their formation was limited to the CG region only (compare Fig. 4b and d). Growth of precipitates is mainly limited by long-range diffusion, fast-growing facets and minimization of anisotropic interface energy and strain energy minimization in case of coherent interfaces [32]. The dominance of these contributions strongly depend on the specific alloy system. The minimization of the volume-specific elastic strain energy is the dominant mechanism in case of incoherent particles, which leads to the formation of needle-shaped Al_6Mn. The diffusion coefficients for diffusion of Mn in Al are $4.8 \cdot 10^{-23} \frac{\mathrm{m}^2}{\mathrm{s}}$ and $1.4 \cdot 10^{-19} \frac{\mathrm{m}^2}{\mathrm{s}}$ for 300 and 375 °C, respectively [33]. It can be seen that the diffusion is four orders of magnitude faster at 375 °C and therefore, the formation of critical Al_6Mn nuclei occurs at a faster rate. At higher temperatures, the faster diffusion rates also facilitate the growth and coarsening of Al_6Mn ($D = 5.3 \cdot 10^{-16} \frac{\mathrm{m}^2}{\mathrm{s}}$ at 550 °C [33]).

As previously reported by Jia et al. [15], Al_3Sc precipitates nucleate at 300 °C, which can be seen in Fig. 4b, where very small Al_3Sc particles are detected by EDS within FG and CG besides the primary, larger Al_3Sc particles. No significant growth of primary Al_3Sc particles was observed in the swaged alloys up to annealing temperatures of 375 °C. This can be associated to the high thermal stability of Zr-

containing Al_3Sc. Fuller et al. [9] investigated the thermal stability of Zr-free and Zr-containing Al_3Sc. Zr improves thermal stability by deteriorating the coherency of Al_3Sc to the Al matrix to up to 375 °C. At higher temperatures, i.e., 550°C the coherency loss of Al_3Sc leads to enhanced coarsening rates of the particles (compare Fig. 4c and e).

Both, Al_6Mn and Al_3Sc are known to shift the occurrence of recrystallization in the LPBF alloy to temperatures above 450 °C [15]. After introducing a high number of defects by swaging, mainly dislocations (see Fig. 6), the first indications of recovery were observed after annealing at 375 °C for 1 h by TEM and XRD. Even though the internal lattice strain after annealing at 375 °C and 550 °C is similar, the microstructure becomes fully equiaxed sole in the 550 °C alloy indicating the onset of recrystallization between the two conditions. Important contributions might be the increased coarsening rates of Al_6Mn and Al_3Sc, which allow grain boundary migration due to the lower number density of larger particles, considering the similar volume fraction at these temperatures. This leads to a fully recrystallized microstructure with equiaxed grains of average (0.88 ± 0.11) µm in size.

4.2 Mechanical properties of the swaged alloys

As can be seen from Fig. 3a and c, hardness and strength of the LPBF alloy are increased by applying a cold working process like rotary swaging up to a true strain of 2.5. The main contributions to strengthening in both alloys are (i) solid solution strengthening σ_{ss}, (ii) grain boundary strengthening σ_{HP}, (iii) precipitation strengthening by nano-sized Al_3Sc σ_{ps} and (iv) dislocation strengthening σ_{dis}. The Peierls stress σ_0 for all investigated alloys is assumed constant and approximated 20 MPa as for pure Al [34]. Hence, it is small compared to the determined yield strengths.

The increase in yield strength by σ_{ss} can be approximated by the following equation [35]:

$$\sigma_{\mathrm{ss}} = \sum_i H_i \, x_i^{n_i} \tag{2}$$

where x_i is the concentration of solute i in atomic percentage, H_i is the strengthening coefficient of solute i and n_i is characteristic exponent of solute i. It is important to note, that (i) during the cold working process Al_3Sc or Al_6Mn particles might be dissolved by localized mechanical alloying (when strain is sufficiently large) [23] and (ii) a localized temperature increase during the cold working process might lead to the formation of additional Al_3Sc and Al_6Mn particles. Both processes would change the volume fraction of additional phases and therefore enrich or deplete the Al solid solution by Sc and Mn and change the contribution by solid solution strengthening. However, no change in volume fraction was observed in this work with respect to the applied microscopic techniques. Furthermore, the lattice parameter of the solid solution remains unaffected by cold working. For this reason, the solid solution strengthening by Mn, Mg and Sc can be assumed similar in the LPBF and swaged alloy. Nevertheless, the supersaturated Al matrix starts to deplete by annealing due to the formation of secondary precipitates. As discussed before, nano-sized Al_3Sc precipitates will form by annealing at 300 °C while Mn and Mg are the remaining contributors to solid solution strengthening [20]. The portion of solid solution strengthening in the swaged alloys will continuously decrease due to the increasing volume fraction of Al_6Mn and Al_3Sc even after annealing at 300 °C and will be on its lowest level after annealing at 375 °C and 550 °C. Bayoumy et al. [20] have estimated a σ_{ss} for the present alloy and processing conditions in the annealing condition (300 °C/6 h) to be 118 and 116 MPa for FG and CG, respectively. Considering the larger volume of Al_3Sc precipitates in the annealed condition compared to the as-fabricated LPBF alloy, σ_{ss} will be slightly higher in the later one. This comes at the expense of σ_{ps} due to the lower number of Al_3Sc precipitates. The determination of σ_{ss} for the swaged and annealed alloys is difficult with respect to the applied methods in this work, due to the high number of nano-sized precipitates even in TEM lamellae. In the view of the increasing volume fraction of Al_3Sc and Al_6Mn during annealing, the contribution of solid solution strengthening will become

smaller in comparison to the other effective strengthening mechanisms in general and to the annealed LPBF alloy in particular. However, since no indication of Mg-containing precipitates were observed in this work and Mg still contributes to σ_{ss}. This is also indicated by the change in lattice parameter (see Fig. 6). By the formation of Al_3Sc and Al_6Mn the lattice parameter increases by annealing at 375 °C and 550 °C to a larger lattice parameter than observed for pure Al (4.049 Å [36]). An increase in lattice parameter above 300 °C can be explained by remaining Mg dissolved in the Al-matrix [37]. The maximum solubility of Sc at 550 °C is reported to be 0.08 at.% [10] and, therefore, no significant contribution to σ_{ss} is expected. Taking the solubility of Mn (0.25 at.% [38]) under equilibrium conditions at 550 °C into account, σ_{ss} for the 550 °C alloy by Mg and Mn is approx. 32 MPa (values of $H = 12.1$ and 54.8 as well as $n = 1.14$ and 1 for Mg and Mn, respectively, were taken from Ref. [34]). This seems negligible for the swaged alloy annealed at 375 °C and 550 °C compared to other strengthening contributions as will be shown later in this discussion.

The grain refinement due to swaging can lead to a substantial increase in strength. In heterogeneous microstructures, a modified linear rule of mixture of two Hall-Petch contributions [14] might be used as approximation of the corresponding strength increment

$$\sigma_{\mathrm{HP}} = \frac{\alpha k}{\sqrt{d_{\mathrm{FG}}}} + \frac{(1-\alpha)k}{\sqrt{d_{\mathrm{CG}}}} \tag{3}$$

where k is the Hall-Petch coefficient (taken as 0.17 MPa $m^{½}$ [39]), α is the area fraction of FG (experimentally determined to be 55%) and d_{FG} and d_{CG} (in width) are the grain sizes of the corresponding regions. In the LPBF condition, σ_{HP} is calculated to be 168 MPa for both, the as-fabricated and the annealed alloy due to the thermally stable microstructure. For the swaged alloy, σ_{HP} increases to 446 MPa by grain refinement due to the cold working process and only slightly decreases to 420 MPa and 367 MPa after annealing at 300 °C and 375 °C, respectively. While the contribution by σ_{HP} to the total strength in the LPBF alloy is only around 40 and 30 % in the as-fabricated and the annealed alloy, respectively, it makes up to approx. 60 % in the swaged and annealed alloy. Even though, σ_{HP} for the 550 °C alloy is just 181 MPa, its total share on the yield strength is around 75 % and, therefore, even higher as in the other swaged alloys. This holds since all other strengthening mechanisms become more or less negligible by annealing at 550 °C, while the grain size still remains small, i.e. (0.88 ± 0.11) µm.

Even though the dislocation density is reported to be higher in LPBF manufactured alloys than in conventional cast metallurgical alloys, σ_{dis} was not considered to contribute to strengthening in previous publications on Al-Sc alloys [14,20,40,41]. Assuming that all internal lattice strains are encountered by dislocations reveals an upper bound of their density as well as an increase thereof by a factor of four by swaging when compared to the LPBF processed sample. This would imply that the contribution of work hardening in this alloy would be doubled [41]. In agreement to the findings of other groups [14,20,41,43] the contribution of work hardening is considered small and will be neglected in what follows.

A high number of secondary Al_3Sc precipitates in the as-fabricated LPBF alloy has been reported previously for several different Al-Mn-Mg-Sc-Zr compositions [14,18,20,41,43]. This is mainly caused by the cyclic heat treatment taking place during the layer-by-layer processing of the alloy. It can be assumed that the contribution by σ_{ps} is similar in both as-fabricated alloys, considering the previously discussed possibility of particle formation and dissolution by the cold working process, which was not observed in this work. Annealing at 300 °C will increase σ_{ps} due to the formation of additional nano-sized Al_3Sc precipitates, as it was shown recently by Bayoumy et al. [20] for the same LPBF alloy investigated here. The authors calculated σ_{ps} to be 258 MPa and 314 MPa for FG and CG, respectively. The difference in FG and CG resulted from a slightly higher number of Al_3Sc precipitates, which was

determined by atom probe tomography APT. The high defect density after swaging can facilitate the formation of precipitates during annealing leading to a higher number of Al_3Sc precipitates compared to the LPBF alloy. For the same reason, these particles can grow faster and lead to a less effective σ_{ps} [44]. This is supported by the larger hardness drop by annealing above 300 °C than for the LPBF alloy, while the grain size remains constant. Recently, Vlach et al. [45] have found, that the formation of needle-shaped Al_6Mn had no significant effect on the hardness of an age hardened Al-Si-Mg-Mn alloy with additions of Sc and Zr. Therefore, we do not expect any additional contributions to strengthening by the formation of Al_6Mn in the alloy investigated in this work.

Overall, it can be assumed that the contribution by σ_{ps} in the LPBF and swaged alloy are comparable for the as-fabricated and annealed alloys. Furthermore, Jia et al. [14] had recently shown that the different strengthening mechanisms add up linearly in this alloy system, so that the yield strength is simply the sum of all contributing strengthening mechanisms. This shows that the drop in strength of the swaged alloy by annealing at temperatures above 300 °C can be attributed to a decrease in (i) σ_{ss} by the depletion of the Al matrix in Sc, Mn and Zr by the formation of precipitates, (ii) σ_{ps} by the growth of precipitates and (iii) σ_{dis} by a reduced dislocation density. The larger drop in strength in the swaged alloy is a direct result of the faster growth rates of precipitates at higher annealing temperatures in the swaged alloy compared to the LPBF alloy.

The absence of work-hardening in the LPBF alloy and the small uniform elongation associated with localized deformation has been recently investigated by Bayoumy et al. [20]. It was attributed to the lack of mobile dislocations and the high number of intermetallic particles along grain boundaries in the FG region of the heterogeneous microstructure. However, we found that work hardening during the tensile test is taking place in the swaged alloys annealed at 375 and 550 °C in this work. Fig. 7 displays the true work-hardening rates plotted against true stress of all alloys investigated by tensile tests here. It can be seen, that all tested LPBF alloys and the swaged alloy annealed at 300 °C show a similar work hardening behavior with only a very brief increase in σ_{t} beyond yielding and before satisfying the Considère criterion necking occurs [46]:

$$\sigma_{\mathrm{t}} = \frac{\mathrm{d}\sigma_{\mathrm{t}}}{\mathrm{d}\varepsilon_{\mathrm{t}}} \tag{4}$$

The calculated work hardening for all those alloys do not significantly deviate from the dashed lines in Fig. 7, which is indicating $\sigma_{0.2}$. Hence, the work hardening capability is low and localization due to mechanical-geometrical instability occurs at low strains. The swaged alloy did not satisfy the Considère criterion due to failure in the grip sections before necking. Low work hardening in Al alloys is mainly due to enhanced dynamic recovery taking place at room temperature caused by high stacking fault energy and cross slip probability.

A clear exception of this trend are the swaged alloys annealed at 375 and 550 °C. The reason for this behavior is difficult to ascertain and not necessarily associated to the cold working process, since the swaged 300 °C condition does not show such a significant deviation from the dashed line. Furthermore, all alloys have a very fine grain size in common, which is generally associated to a lack of work hardening capability in Al alloys with ultra-fine grain structures, such as commercial 1100 Al [47] AA1050 [48,49] and AA5754 [50]. It has been reported previously in Refs. [51,52] that introducing a significant number of coarse grains to form a bimodal microstructure increases the work hardening capability of such alloys. It is worth noting, that all alloys except the swaged 550 °C already exhibit a bimodal microstructure even after swaging, as can be seen in Fig. 5. However, the heterogeneous microstructure in the LPBF alloys investigated here, possesses grain sizes of around 1 µm and below and is considerably finer in the swaged alloys by one order of magnitude. Therefore, a bimodal microstructure is not expected to increase the work hardening capability of the alloys here, most likely

due to the very small grain size of CG. The criteria that distinguish the swaged alloys annealed at 375 and 550 °C from all other alloys is (i) the significantly higher amount of Al_3Sc and Al_6Mn particles and a therefore a smaller amount of Mn and Sc dissolved in solid solution and (ii) the transition from Al_3Sc particles that can be cut to one that cannot be cut [52]. Recently, Ma et al. [54] have investigated the mechanical behavior of a LPBF Al-Mg-Sc-Zr alloy after subsequent cold rolling. This alloy contained around 0.5 wt.% Mn. Even though, Ma et al. did not focus on the work hardening capability of this alloy, some work hardening is taking place and no yield phenomenon causing small uniform elongation was observed independent of the processing of the alloy. It is noteworthy here, that the average grain size of the cold-worked, and annealed alloy was above 1 µm. The work hardening capability could then be linked to the absence of Mn in solid solution, which mainly contains Mg as dissolved element in Al at annealing temperatures of 375 °C and above in the swaged condition. Fazeli et al. [55] found that an increased particle size of Al_3Sc in an Al-Mg-Sc alloy enhances the work hardening capability. This is attributed to the transition of shearable to non-shearable Al_3Sc particles by growth to a critical diameter at high temperatures, at which misfit dislocations are formed in the Al/Al_3Sc interface [56]. Several authors have reported on the critical diameter for coherency loss to be ranging from 28 to 40 nm in binary Al-Sc with Sc contents of 0.12 to 0.5 wt.% [16,57-61]. The growth of Al_3Sc to this critical diameter was only observed at temperatures above 400 °C in case of binary Al-Sc alloys manufactured by casting [58]. As the results of the present work reveal, the precipitation and growth kinetics of Al_3Sc are enhanced by cold working of the LPBF alloy. Therefore, it can be expected that the critical diameter of Al_3Sc to transition from shearable to non-shearable is reached at lower temperatures and shorter heat treatment times in the swaged alloy heat treated at 375 and 550 °C for 1 h. However, even modelling of the strength of metallic materials with such complex hierarchical microstructures and with such superposition of various strengthening contribution is challenging taking the non-linear superposition and uncertainties of experimental characterization into account [62]. Hence, proper modeling of the work hardening capability and investigation of the effect of a potential transition from particle cutting to Orowan mechanism might be restricted to simple model systems.

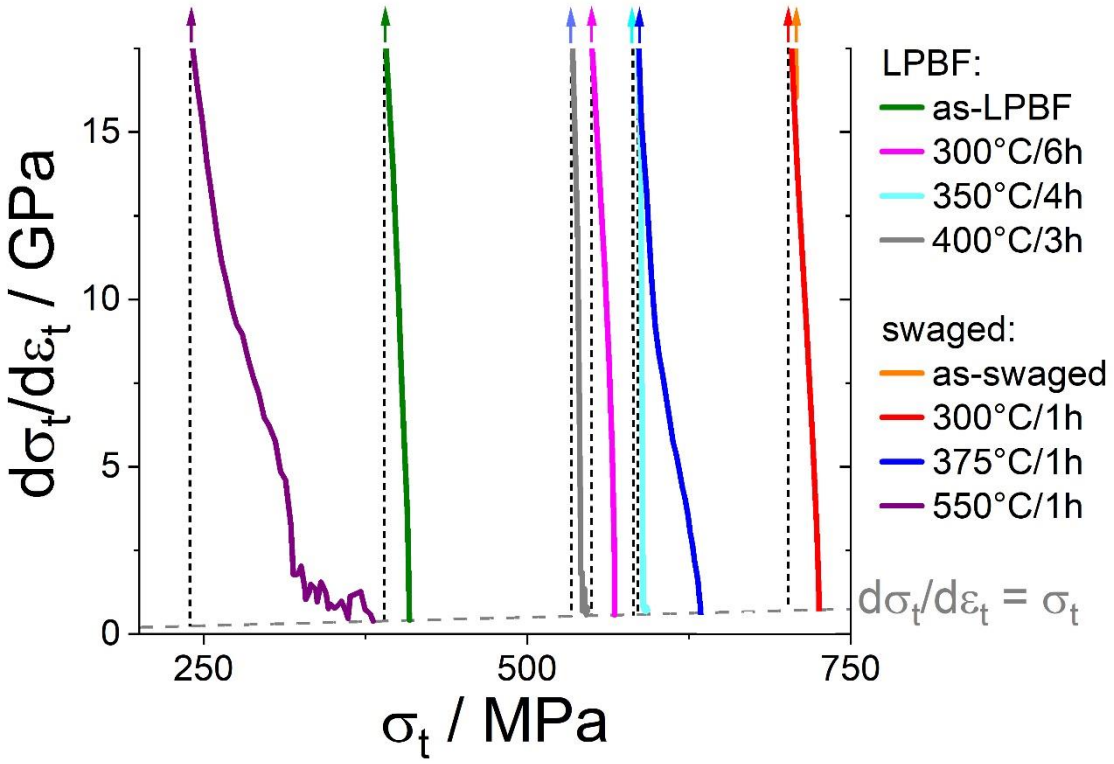

Figure 7: True work hardening rate $\frac{d\sigma_t}{d\varepsilon_t}$ as a function of σ_t. The dashed line indicates the Considère criterion for the onset of mechanical-geometrical instability.

5. Conclusions

An Al-Mn-Mg-Sc-Zr alloy was additively manufactured and deformed by rotary swaging. Subsequent aging yields significant acceleration of aging kinetics and improvement of uniform elongation by enhanced work hardening capability for annealing temperatures above 300 °C while strength is only moderately affected. The following conclusions can be drawn from the present investigations:

- Cold work up to true strain of 2.5 does not destroy the heterogeneous microstructure of the LPBF alloy.
- Precipitation and coarsening kinetics are significantly improved by cold working prior to aging treatment, e.g. peak hardness is obtained at lower temperatures and shorter durations. Peak hardness and peak strength are superior for the cold worked condition over the LPBF alloy.
- The uniform elongation significantly increases by heat treatment of the cold worked alloy, while maintaining high strength compared to the peak aged LPBF condition. Enhanced ability for uniform plastic deformation is achieved by improved work hardening capability presumably by the transition from precipitates that are cut to particles circumvented by the Orowan mechanism.
- The main contribution to strengthening of the cold-worked alloy is found to be the increased σ_{HP} by the finer microstructure.
- The fine-grained heterogeneous microstructure remains stable up to heat treatment at 375 °C for 1h. Precipitation is completed for 375°C and 1h and evidence for recovery is obtained. Beyond that recrystallization and coarsening occurs.

Acknowledgement

The authors gratefully acknowledge financial support from the Australian Research Council grant number IH130100008 “Industrial Transformation Research Hub for Transforming Australia's Manufacturing Industry through High Value Additive Manufacturing”. YME additionally acknowledge financial support by the Deutsche Forschungsgemeinschaft (DFG) within the framework of GRK 2561 MatCom-ComMat. This work was partly carried out with the support of the Karlsruhe Nano Micro Facility (KNMFi, www.knmf.kit.edu), a Helmholtz Research Infrastructure at Karlsruhe Institute of Technology (KIT, www.kit.edu).

References

[1] D. Koutny, D. Skulina, L. Pantělejev, D. Paloušek, B. Lenczowski, F. Palm, A. Nick, Processing of Al-Sc aluminium alloy using SLM technology, Procedia CIRP 74 (2018) 44-48. https://doi.org/10.1016/j.procir.2018.08.027.

[2] A.B. Spierings, K. Dawson, K. Kern, F. Palm, K. Wegener, SLM-processed Sc- and Zr- modified Al-Mg alloy: Mechanical properties and microstructural effects of heat treatment, Mater. Sci. Eng. A 701 (2017) 264-273. https://doi.org/10.1016/j.msea.2017.06.089.

[3] A.B. Spierings, K. Dawson, M. Voegtlin, F. Palm, P.J. Uggowitzer, Microstructure and mechanical properties of as-processed scandium-modified aluminium using selective laser melting, CIRP Annals 65 (2016) 213-216. https://doi.org/10.1016/j.cirp.2016.04.057.

[4] Z. Yin, Q. Pan, Y. Zhang, F. Jiang, Effect of minor Sc and Zr on the microstructure and mechanical properties of Al-Mg based alloys, Mater. Sci. Eng. A 280 (2000) 151-155. https://doi.org/10.1016/S0921-5093(99)00682-6.

[5] S. Costa, H. Puga, J. Barbosa, A.M.P. Pinto, The effect of Sc additions on the microstructure and age hardening behaviour of as cast Al-Sc alloys, Mater. Design 42 (2012) 347-352. https://doi.org/10.1016/j.matdes.2012.06.019.

[6] F. Wang, D. Qiu, Z.-L. Liu, J.A. Taylor, M.A. Easton, M-X. Zhang, The grain refinement mechanism of cast aluminium by zirconium, Acta Mater. 61 (2013) 5636-5645. https://doi.org/10.1016/j.actamat.2013.05.044.

[7] V. Ocenasek, M. Slamova, Resistance to recrystallization due to Sc and Zr addition to Al-Mg alloys, Mater. Charact. 47 (2001) 157-162. https://doi.org/10.1016/S1044-5803(01)00165-6.

[8] Y. Harada, D.C. Dunand, Creep properties of Al3Sc and Al3(Sc, X) intermetallics, Acta Mater. 48 (2000) 3477-3487. https://doi.org/10.1016/S1359-6454(00)00142-7.

[9] C.B. Fuller, D.N. Seidman, Temporal evolution of the nanostructure of Al(Sc,Zr) alloys: Part II-coarsening of Al3($Sc_{1-x}Zr_x$) precipitates, Acta Mater. 53 (2005). https://doi.org/10.1016/j.actamat.2005.08.015.

[10] J.L. Murray, The Al-Sc (Aluminum-Scandium) System, J. Phase Equilib. 19 (1998) 380. https://doi.org/10.1361/105497198770342120.

[11] M. Ma, Z. Wang, X. Zeng, A comparison on metallurgical behaviors of 316L stainless steel by selective laser melting and laser cladding deposition, Mater. Sci. Eng. A 685 (2017) 265-273. https://doi.org/10.1016/j.msea.2016.12.112.

[12] M. Tang, P.C. Pistorius, S. Narra, J.L. Beuth, Rapid Solidification: Selective Laser Melting of AlSi10Mg, JOM 68 (2016) 960-966. https://doi.org/10.1007/s11837-015-1763-3.

[13] E.A. Jägle, Z. Sheng, L. Wu, L. Lu, J. Risse, A. Weisheit, D. Raabe, Precipitation Reactions in Age-Hardenable Alloys During Laser Additive Manufacturing, JOM 68 (2016) 943-949. https://doi.org/10.1007/s11837-015-1764-2.

[14] Q. Jia, P. Rometsch, P. Kürnsteiner, Q. Chao, A. Huang, M. Weyland, L. Bourgeois, X. Wu, Selective laser melting of a high strength Al-Mn-Sc alloy: Alloy design and strengthening mechanisms, Acta Mater. 171 (2019) 108-118. https://doi.org/10.1016/j.actamat.2019.04.014.

[15] Q. Jia, F. Zhang, P. Rometsch, J. Li, J. Mata, M. Weyland, L. Bourgeois, M. Sui. X. Wu, Precipitation kinetics, microstructure evolution and mechanical behavior of a developed Al-Mn-Sc alloy fabricated by selective laser melting, Acta Mater. 193 (2020) 239-251. https://doi.org/10.1016/j.actamat.2020.04.015.

[16] M.J. Jones, F.J. Humphreys, Interaction of recrystallization and precipitation: The effect of Al_3Sc on the recrystallization behaviour of deformed aluminium, Acta Mater. 8 (2003) 2149-2159. https://doi.org/10.1016/S1359-6454(03)00002-8.

[17] D. Schliephake, D. Bayoumy, S. Seils, C. Schulz, A. Kauffmann, X. Wu, A.J. Huang, Mechanical behavior at elevated temperatures of an Al-Mn-Mg-Sc-Zr alloy manufactured by selective laser metling, Mater. Sci. Eng. A 831 (2022) 142032. https://doi.org/10.1016/j.msea.2021.142032.

[18] A.B. Spierings, K. Dawson, T. Heeling, P.J. Uggowitzer, R. Schäublin, F. Palm, K. Wegener, Microstructural features of Sc- and Zr-modified Al-Mg alloys processed by selective laser melting, Mater. Design 115 (2017) 52-63. https://doi.org/10.1016/j.matdes.2016.11.040.

[19] D. Bayoumy, D. Schliephake, S. Dietrich, X.H. Wu, Y.M. Zhu, A.J. Huang, Intensive processing optimization for achieving strong and ductile Al-Mn-Mg-Sc-Zr alloy produced by selective laser melting, Mater. Design 198 (2021) 109317. https://doi.org/10.1016/j.matdes.2020.109317.

[20] D. Bayoumy, K. Kwak, T. Boll, S. Dietrich, D. Schliephake, J. Huang, K. Takashima, X. Wu, Y. Zhu, A. Huang, Origin of non-uniform plasticity in a high-strength Al-Mn-Sc based alloy produced by laser powder bed fusion, J. Mater. Sci. Tech. 103 (2022) 121-133. https://doi.org/10.1016/j.jmst.2021.06.042.

[21] J.B. Nelson, D.P. Riley, An experimental investigation of extrapolation methods in the derivation of accurate unit-cell dimensions of crystals, Proc. Phys. Soc. 57 (1945) 160. https://doi.org/10.1088/0959-5309/57/3/302.

[22] G.K. Willamson, R.E. Smallan, Dislocation densities in some annealed and cold-worked metals from measurements on the X-ray debye-scherrer spectrum, Philos. Mag. 1 (1956) 34-46. https://doi.org/10.1080/14786435608238074.

[23] X. Sauvage, F. Wetscher, P. Pareige, Mechanical alloying of Cu and Fe induced by severe plastic deformation of a Cu-Fe composite, Acta Mater. 53 (2005) 2127-2135. https://doi.org/10.1016/j.actamat.2005.01.024.

[24] U.F. Kocks, C.N. Tomé, H.-R. Wenk, Texture and Anisotropy: Preferred Orientations in Polycrystals and their Effect on Materials Properties, Cambridge University Press 2000.

[25] T. Marr, J. Freudenberger, A. Kauffmann, J. Scharnweber, C.-G. Oertel, W. Skrotzki, U. Kühn, J. Eckert, U. Martin, L. Schultz, Damascene Light-Weight Metals, Adv. Eng. Mater. 12 (2010) 1191-1197. https://doi.org/10.1002/adem.201000198.

[26] N. Hansen, Cold deformation microstructures, Mater. Sci. Tech. Ser. 6 (1990) 1039-1047. https://doi.org/10.1179/mst.1990.6.11.1039.

[27] R. Kaibyshev, S. Malopheyev, Mechanisms of Dynamic Recrystallization in Aluminum Alloys, Mater. Sci. Forum 794-796 (2014) 784-789. https://doi.org/10.4028/www.scientific.net/MSF.794-796.784.

[28] P.J. Apps, M. Berta, P.B. Prangnell, The effect of dispersoids on the grain refinement mechanisms during deformation of aluminium alloys to ultra-high strains, Acta Mater. 53 (2005) 499-511. https://doi.org/10.1016/j.actamat.2004.09.042.

[29] Y. Huang, J.D. Robson, P.B. Prangell, The formation of nanograined structures and accelerated room-temperature theta precipitation in a severly deformed Al-4wt.% Cu alloy, Acta Mater. 58 (2010) 1643-1657. https://doi.org/10.1016/j.actamat.2009.11.008.

[30] P. Chekhonin, J. Scharnweber, M. Scharnweber, C.-G. Oertel, T. Hausöl, H.W. Höppel, J. Jaschinski, T. Marr, W. Skrotzki, Mechanical properties of aluminium laminates produced by accumulative roll bonding, Cryst. Res. Technol. 48 (2013) 532-537. https://doi.org/10.1002/crat.201300121.

[31] S. Grosse, C. Hutchinson, M. Goune, R. Banerjee, Additive manufacturing of metals: a brief review of the characteristic microstructures and properties of steels, Ti-6Al-4V and high entropy alloys, Sci. Technol. Adv. Mat. 18 (2017) 584-610. https://doi.org/10.1080/14686996.2017.1361305.

[32] R.F. Sekerka, Theory of Crystal Growth Morphology, in: G. Müller, J.-J. Métois, P. Rudolph (Eds.) Crystal Growth – From Fundamentals to Technology, 2004, pp. 55-93. https://doi.org/10.1016/B978-044451386-1/50005-2.

[33] G. Rummel, T. Zumkley, M. Eggersmann, K. Freitag, H. Merer, Diffusion of Implanted 3d-Transition Elements in Aluminium Part I: Temperature Dependence, Int. J. Mater. Res. 86 (1995) 122-130. https://doi.org/10.1515/ijmr-1995-860208.

[34] Ø. Ryen, B. Holmedal, O. Nijs, E. Sjölander, H.-E. Ekström, Strengthening mechanisms in solid solution aluminum alloys, Metall. Mater. Trans. A 37 (2006) 1999-2006. https://doi.org/10.1007/s11661-006-0142-7.

[35] L.A. Gypen, A. Deruyettere, Multi-component solid solution hardening, J. Mater. Sci. 12 (1977) 1028-1033. https://doi.org/10.1007/BF00540987.

[36] H.M. Otte, W.G. Montague, D.O. Welch, X-Ray Diffractometer Determination of the Thermal Expansion Coefficient of Aluminum near Room Temperature, J. Appl. Phys. 34 (1963) 3149. https://doi.org/10.1063/1.1729148.

[37] J.L. Murray, The Al-Mg (Aluminum-Magnesium) system, J. Phase Equilib. 3 (1982) 60. https://doi.org/10.1007/BF02873413.

[38] Y. Minamino, T. Yamane, H. Araki, N. Takeuchi, Y.-S- Kang, Y. Miyamoto, T. Okamoto, Solid solubilities of manganese and titanium in aluminum at 0.1 MPa and 2.1 GPa, Metall. Mater. Trans. A 22 (1991) 783-786. https://doi.org/10.1007/BF02670301.

[39] J.R. Croteau, S. Griffiths, M.D. Rossell, C. Leinenbach, C. Kenel, V. Jansen, D.N. Seidman, D.C. Dunand, N.Q. Vo, Microstructure and mechanical properties of Al-Mg-Zr alloys processed by selective laser melting, Acta Mater. 153 (2018) 35-44. https://doi.org/10.1016/j.actamat.2018.04.053

[40] A.B. Spierings, K. Dawson, P.J. Uggowitzer, K. Wegener, Influence of SLM scan-speed on microstructure, precipitation of Al_3Sc particles and mechanical properties in Sc- and Zr-modified Al-Mg alloys, Mater. Design 140 (2018) 134-143. https://doi.org/10.1016/j.matdes.2017.11.053.

[41] R. Li, M. Wang, Z. Li, P. Cao, T. Yuan, H. Zhu, Developing a high-strength Al-Mg-Si-Sc-Zr alloy for selective laser melting: Crack-inhibiting and multiple strengthening mechanisms, Acta Mater. 193 (2020) 83-98. https://doi.org/10.1016/j.actamat.2020.03.060.

[42] G.I. Taylor, The mechanism of plastic deformation of crystals. Part I. – Theoretical, P. r. Soc. A 145 (1934) 362-387. https://doi.org/10.1098/rspa.1934.0106.

[43] X.F. Shen, Z.Y. Cheng, C.G. Wang, H.F. Wu, Q. Yang, G.W. Wang, S.K. Huang, Effect of heat treatments on the microstructure and mechanical properties of Al-Mg-Sc-Zr alloy fabricated by selective laser melting, Opt. Laser Technol. 143 (2021) 107312. https://doi.org/10.1016/j.optlastec.2021.107312.

[44] D.S. D'Antuono, J. Gaies, W. Golumbfskie, M.L. Taheri, Direct measurement of the effect of cold rolling on β phase precipitation kinetics in 5xxx series aluminum alloys, Acta Mater. 123 (2017) 264-271. https://doi.org/10.1016/j.actamat.2016.10.060.

[45] M. Vlach, J. Čižek, B. Smola, O. Melikhova, M. Vlček, V. Kodetová, H. Kudrnová, P. Hruška, Heat treatment and age hardening of Al-Si-Mg-Mn commercial alloy with addition of Sc and Zr, Mater. Charact. 129 (2017) 1-8. https://doi.org/10.1016/j.matchar.2017.04.017.

[46] G. Gottstein , Physical Foundations of Materials Science, Springer Science & Business Media, 2004. https://doi.org/10.1007/978-3-662-09291-0

[47] N. Tsuji, Y. Ito, Y. Saito, Y. Minamino, Strength and ductility of ultrafine grained aluminum and iron produced by ARB and annealing, Scr. Mater. 47 (2002) 893-899. https://doi.org/10.1016/S1359-6462(02)00282-8.

[48] C.Y. Yu, P.W. Kao, C.P. Chang, Transition of tensile deformation behaviors in ultrafine-grained aluminum, Acta Mater. 53 (2005) 4019-4028. https://doi.org/10.1016/j.actamat.2005.05.005.

[49] P.L. Sun, C.Y. Yu, P.W. Kao, C.P. Chang, Influence of boundary characters on the tensile behavior of sub-micron-grained aluminum, Scr. Mater. 52 (2005) 265-269. https://doi.org/10.1016/j.scriptamat.2004.10.022.

[50] D.J. Lloyd, H. Jin, Inhomogeneous yielding and work hardening of a fine grained Al-Mg alloy, Mater. Sci. Eng. A 585 (2013) 455-459. https://doi.org/10.1016/j.msea.2013.07.044.

[51] H. Jin, D.J. Lloyd, Effect of a duplex grain size on the tensile ductility of an ultra-fine grained Al-Mg alloy, AA5754, produced by asymmetric rolling and annealing, Scr. Mater. 50 (2004) 1319-1323. https://doi.org/10.1016/j.scriptamat.2004.02.021.

[52] H. Jin, M. Gallerneault, D.J. Lloyd, Low Work Hardening And Its Mitigation In Ultra-Fine Grained Aluminum Alloys, In: H. Weiland, A.D. Rollett, W.A. Cassada (Eds.), Proceedings of International Conference on Al Alloys-13, TMS ,2012, pp. 1741-1752. https://doi.org/10.1002/9781118495292.ch260.

[53] Ø. Ryen, B. Holmedal, K. Marthinsen, T. Furu, Precipitation, strength and work hardening of age hardened aluminium alloys, IOP Conf. Ser.: Mater. Sci. Eng. 89 (2015) 012013. DOI:10.1088/1757-899X/89/1/012013.

[54] R. Ma, C. Peng, Z. Cai, R. Wang, Z. Zhou, X. Li, X. Cao, Enhanced strength of selective laser melted Al-Mg-Sc-Zr alloy by cold rolling, Mater. Sci. Eng. A 775 (2020) 138975. https://doi.org/10.1016/j.msea.2020.138975

[55] F. Fazeli, W.J. Poole, C.W. Sinclair, Modeling the effect of Al_3Sc precipitates on the yield stress and work hardening of an Al-Mg- Sc alloy, Acta Mater. 56 (2008) 1909-1918. https://doi.org/10.1016/j.actamat.2007.12.039

[56] J. Røset, N. Ryum, Some comments on the misfit and coherency loss of Al3Sc particles in Al-Sc alloys, Scr. Mater. 52 (2005) 1275-1279. https://doi.org/10.1016/j.scriptamat.2005.02.023.

[57] C. Watanabe, T. Kondo, R. Monzen, Coarsening of Al_3Sc precipitates in an Al-0.28 wt pct Sc alloy, Metall. Mater. Trans A 35 (2004) 3003-3008. https://doi.org/10.1007/s11661-004-0247-9.

[58] J.W. Riddle, T.H. Sanders Jr., Recrystallisation Performance of AA7050 Varied with Sc and Zr, Mater. Sci. Forum 331-337 (2000) 799-804. https://doi.org/10.4028/www.scientific.net/MSF.331-337.799.

[59] S. Iwamura, Y. Miura, Loss in coherency and coarsening behavior of Al_3Sc precipitates, Acta Mater. 52 (2004) 591-600. https://doi.org/10.1016/j.actamat.2003.09.042.

[60] E.A. Marquis, D.N. Seidman, Nanoscale structural evolution of Al3Sc precipitates in Al(Sc) alloys, Acta Mater. 49 (2001) 1909-1919. https://doi.org/10.1016/S1359-6454(01)00116-1.

[61] M.E. Drits, L.S. Toropova, U.G. Bikov, Alloy Al-Sc Age-Hardeing Kinetics, Retrospective Collection 1, Trans. Tech. Publications (1983) 616-623.

[62] S. Seils, A. Kauffmann, F. Hinrichs, D. Schliephake, T. Boll, M. Heilmaier, Temperature dependent strengthening contributions in austenitic and ferritic ODS steels, Mater. Sci. Eng. A 786 (2020) 139452